SCIEPublish

Article

Porous 430L Stainless Steel as a Support Layer for Planar Solid Oxide Cells: Effect of Porosity on Mechanical Properties

Yifei Yan [1], Dhruv Bajaj [2], Daolun Chen [2] and Olivera Kesler [1,*]

[1] Department of Mechanical and Industrial Engineering, University of Toronto, 5 King's College Road, Toronto, ON M5S 3G8, Canada; yf.yan@mail.utoronto.ca (Y.Y.)

[2] Department of Mechanical, Industrial and Mechatronics Engineering, Toronto Metropolitan University, 350 Victoria Street, Toronto, ON M5B 2K3, Canada; dhruv.bajaj@torontomu.ca (D.B.); dchen@torontomu.ca (D.C.)

* Corresponding author. E-mail: kesler@mie.utoronto.ca (O.K.)

Received: 30 October 2024; Accepted: 23 December 2024; Available online: 31 December 2024

ABSTRACT: Porous 430L stainless steel components fabricated via tape casting underwent mechanical testing for potential in-vehicle application as mechanical supports of solid oxide cells. Tests included three-point bending up to 5% strain to assess flexural strength, yield strength, Young's modulus, indentation hardness, and microstructural characterization. This study aimed to establish the relationship between pore former size and volume fraction and the resulting yield strength. It also compared sintered material without pore former, focusing on the influence of a wide range of porosity of up to 46.5%. The materials exhibited an inverse relationship for Young's modulus, hardness and yield strength as a function of porosity. The lowest flexural yield strength obtained was approximately 120 MPa at the highest porosity of 46.5%, meeting the requirement of 59 MPa for the bipolar plates of existing proton-exchange membrane fuel cells.

Keywords: Stainless steel; Three-point bending; Porosity; SOC substrate; EBSD; Mechanical properties

1. Introduction

Transportation is responsible for 15% of total greenhouse gas emissions and approximately 23% of global energy-related CO_2 emissions [1]. The shift from traditional fossil fuel vehicles to zero-emission ones is crucial in mitigating the impact of rising global temperatures. Fuel cell technology is a viable solution, particularly for heavy-duty long-haul trucks, while batteries offer more advantages for small passenger vehicles [2–4]. With the higher fuel energy density compared to batteries, fuel cell vehicles and the corresponding fuel storage tanks reduce onboard costs and space related to energy storage. However, additional space and weight requirements remain for the cell stacks for power generation. For small and compact passenger vehicles, this additional space requirement for the cell stack beside the fuel tank makes the fuel cell stack a less favoured solution. As the demand for onboard energy storage increases for heavier vehicles, the weight of batteries increases much faster than increasing fuel. Hence, using higher energy density storage media, fuel cell systems are especially advantageous for large, heavy vehicles with long operation distances [5,6]. In addition, larger vehicles have fewer space restrictions for cell stacks. This is more forgivable to high-temperature cells that require additional insulation that is often about 10-cm thick but provides higher thermal efficiency [7].

Within fuel cell technologies, proton exchange membrane fuel cells have been extensively studied and commercialized because of their high volumetric energy density, good fracture toughness, and short start-up time [8]. Solid oxide fuel cells are more often used for stationary power generation due to higher energy conversion efficiency of up to 70% [7,9] and flexibility of fuel: from hydrogen to carbon-containing fuel [10] and ammonia [11]. This fuel flexibility allows solid oxide cells (SOCs) to have the option of using liquid fuels such as methanol or gasoline rather than hydrogen, which can only be stored in a compressed state with a limited volumetric energy density range from 30–50 kg H_2/m^3 [12]. Various liquid-hydrocarbon- or alcohol-fuelled SOC systems have been reported [13–15]; if the fuel is generated from renewable sources, the vehicles that operate on those fuels are also zero-emission.

https://doi.org/10.70322/htm.2024.10011

Traditional SOCs are used for stationary power generation instead of vehicle applications because of long start-up times [16], redox cycling intolerance [17], and low fracture toughness due to ceramic or cermet construction. Such obstacles can be overcome by replacing the ceramic or cermet layer that provides mechanical support with a porous metal layer [18–20]. Specifically, ferritic stainless steel with a good match of thermal expansion coefficient to that of 8 mol% yttria-stabilized zirconia has been extensively studied for such applications. Those materials include 400 series stainless steel [21,22] and commercially developed high Cr alloys such as 1C44Mo20 [23] and Crofer 22-APU [24]. A metal's higher fracture toughness and thermal conductivity allow for faster temperature ramping of cells compared to cermet-supported designs without thermal shock and for resilience to external stress [25]. Since the SOC stacks often operate at high temperatures ranging from 600 to 800 °C, high oxidation resistance of all cell materials is required. Even if the metal support layer is adjacent to the fuel electrode, the water vapour formed due to the fuel oxidation reaction can still oxidize stainless steel [26] and vaporize chromium oxide by forming more volatile hydroxide [27].

The fabrication methods of this metal layer include, but are not limited to: laser drilling [19], dry powder metallurgy [28], or the application of suspension-based wet ceramic methods such as slip casting [29], screen printing [30], or tape casting [31] adapted for the processing of metal powders. The wet ceramic methods typically involve preparing a homogeneous suspension of metal powder and pore former and other additives such as binder and dispersants [32]. The slurry is then cast into desired shapes, and the shape is fixed after the solvent is removed. The pore former is a filler material in the green body, decomposing at higher temperatures and leaving porosity in a cast green body. After organic content removal, often in an oxidative environment, the steel powder is sintered at a higher temperature in a protective atmosphere to achieve the desired density [33].

To improve the longevity of metal-supported cells, multiple approaches have been studied, including developing a more corrosion-resistant alloy by increasing Cr content and stabilizing the Cr in Fe solution by adding other minor elements such as Nb [34]. Developing protective coatings on steel support surfaces also effectively slows down oxidation by applying either coating precursor element salt solutions [35,36] or by electroplating [37]. Improved oxidation resistance has also been achieved through microstructural modification, such as decreasing the surface area of the metal phase by using rougher powder for sintering [38].

From the material standpoint, the metal support should have a combination of high gas permeability [21], mechanical strength [39], and low surface area [38]. The support layer itself should provide sufficient support to prevent the ceramic electrodes and electrolyte layers from fracturing; typically, a thickness ranging from 0.5 to 1.5 mm is required [22,40,41]. The material must also be porous to allow gas transport to the electrode with a minimal concentration gradient for adequate cell performance at a high current density [39]. However, more porosity also increases the support surface area to volume ratio, which accelerates Cr loss and can lead to subsequent breakaway oxidation due to Cr depletion [42,43]. Increased porosity and larger individual pore sizes also tend to decrease the material's mechanical properties, such as hardness, flexural strength, and fatigue strength [44,45]. To mitigate these problems, the pore structure should be less tortuous and better interconnected for a given porosity to achieve higher gas permeability, lower surface area, and improved mechanical properties.

There are no established mechanical testing standards for solid oxide cells in-vehicle applications. Considering the typical planar cell geometry, if a cell were to fail due to mechanical deformation caused by bending stress, it would likely occur where the most prominent deformation is present. This location is at the cell center since the cells are constrained from deformation near the edges by compression applied to establish reliable sealing. In contrast, the center is not as well-supported with metal meshes inserted between the cells and interconnects to serve as current collectors. Therefore, in a situation where a pressure differential exists between the air and fuel sides of the cells, a thin interconnect plate with a flexible mesh used for electrical contact could deform in bending. In such cases, flexural testing is more suitable than purely compressive or tensile testing, since the bending failure load is lower than the compressive failure load for ceramic and metal materials of a given geometry. When assembled into stacks or under load or impact, the most vulnerable scenario for cell failure due to mechanical deformation is when the load force is perpendicular to the cell plane. Therefore, we use three-point bending methods to test metal supports in this study, following ASTM D790 and ASTM C1161 standards. Additionally, micro-hardness testing was performed to gain a more detailed understanding of the mechanical properties. Since SOCs have not yet been commonly used in vehicle applications, target properties for such applications for PEMFC bipolar plates were compared to provide context for the mechanical properties of this study. Based on published PEMFC bi-polar plate mechanical property requirements, the flexural strength of layers within a stack must be greater than 59 MPa for vehicle application [46]. While SOC planar stacks also typically utilize bi-polar plate interconnects that would provide some mechanical support to the cells in the stack, the metal support

layer for each cell still needs to be sufficiently resistant to bending and plastic deformation to protect the thin, brittle electrolyte layer from fracturing.

In previous studies, metal supports were fabricated via wet-ceramic-based methods [47] or die-pressing [20]. However, these methods used relatively large metal powder particles, leading to inter-particle porosity that increased the surface area to volume ratio without significantly contributing to gas permeability due to high tortuosity and dead ends. A novel combination of steel powder size and pore former size selection was tested in an aqueous slurry system with a wet-ceramic-based method in our previous study, exploring the effects of pore former particle size and volume fraction on substrate properties relevant to fuel cell electrochemical performance [48].

This work aims to characterize the mechanical properties of the porous metal supports developed previously, focusing on properties relevant to vehicle applications. The study also includes dense material as part of a baseline comparison and to provide material property information that can serve as a design reference for the interconnect layer between cells in a stack.

2. Materials and Methods

2.1. Materials

430L stainless steel powder (Sandvik Osprey Ltd., Neath, UK) with $d_{0.9} < 10$ μm was used to fabricate the metal supports. Poly(methyl methacrylate) (PMMA) beads with two different sizes of $d_{0.9} < 20$ μm (Lamberti, Skedsmokorset, Norway) and 60 μm (Huaqing Natural Ingredients, Xi'An, China) were used as the pore former (PF). The aqueous tape casting slurry used polyvinyl alcohol (PVA, 98–99% hydrolyzed low molecular weight, Thermo Scientific, Waltham, USA) as the binder, polyethylene imine (PEI, *M*w~2000, Sigma Aldrich, St, Louis, USA) as the dispersant, and anti-foam 204 (Sigma Aldrich) as the defoamer. The slurry compositions used in this study are listed in Table 1. More details about developing the slurry preparation and tape casting procedures can be found in the previous work [33].

Table 1. Four slurry compositions were used to fabricate seven studied samples with various porosities. The pore former fraction is based on total particle volume, and samples made with two different size distributions of PF particles were used for each PF volume fraction.

	430L SS (g)	PMMA (g)	PVA (mL)	PEI (mL)	Antifoam 204 (mL)	Water (mL)
No PF	57.75	0	5	0.5	0.15	5
35 vol% PF	37.54	3.10	5	0.5	0.15	5
45 vol% PF	31.76	3.98	5	0.5	0.15	5
55 vol% PF	25.99	4.87	5	0.5	0.15	5

2.2. Processing Methods

The green tapes were cast using a doctor blade with a 100 mm width and a 1.5 mm gap height at a speed of 2 mm/s. The as-cast tapes were left in the air without forced convection on a commercial sprouting mattress with a setpoint of 38 °C. Dry green tapes were cut into strips roughly 3 mm wide and 30 mm long by hand with a saw blade before thermal processing.

The green strips underwent an organic removal step in an intermediate temperature tube furnace (Thermolyne 79325, Thermo Fisher, Waltham, USA) with air flowing at 500 standard cubic centimetres per minute (SCCM) up to 400 °C. At this temperature, the air was purged by nitrogen and the flowing gas was switched to 200 SCCM H_2, followed by a 4-h dwelling at 850 °C. The final sintering was performed in another tube furnace (1632 12HT, CM Furnaces Inc., Bloomfield, USA) at 1200 °C for 4 h with 500 SCCM H_2. The organic burnout process in the first furnace will leave residues such as carbon and tar inside the tube; the tube is made of material resistant to carbon deposition (silica glass) but will not withstand high sintering temperatures of steel. The high-temperature furnace uses alumina to withstand high temperatures, but carbon deposition will degrade the life expectancy. The heating elements of the high-temperature furnace are also not designed to withstand extended holds at low to moderate temperatures, such as those needed to burn out the organic phases. Alumina plates were used to hold the samples in the furnaces. After sintering, some samples did not have good flatness. Those samples were straightened by cold work and annealed together with straight ones in the high-temperature tube furnace up to 1200 °C without dwelling. The cooling rate was 1.7 °C/min when the furnace temperature was above 800 °C and 5 °C/min when the temperature was below 800 °C. The sintered strips were not polished, as plasma spraying requires the substrate to have adequate surface roughness for effective material deposition [23].

To prepare the samples for image analysis, the specimens were mounted in epoxy, ground, and polished with diamond paste fine to 1 μm. Etching was done with HF (48 wt%, Sigma Aldrich, St. Louis, USA)-HNO_3 (70 wt%, BDH, Radnor, USA)

solution diluted with water at an 8:10:82 volume ratio, respectively. The sample was placed in the solution for 4 min to obtain observable grain structure.

2.3. Characterization Methods

Both optical microscopy (Axio Scope, Carl Zeiss, Oberkochen, Germany) and scanning electron microscopy (JSM-6380LV, JEOL, Akishima, Japan) were used to examine the sample structure. Porosity was determined by image analysis using ImageJ software to count the area fraction of dark pixels over the total image area. Electron backscatter diffraction (EBSD) scans were collected using Oxford integrated AZtecHKL advanced software. X-ray photoelectron spectroscopy (XPS, K-Alpha XPS system, Thermo Fisher) measured residue carbon on green tape after outgassing. The samples were prepared by ion milling to remove contamination from the air before XPS.

Three-point bending (TPB) tests were conducted on a three-point bending stage with a 20 mm span. A computerized Instron 8801 system was used to control the motion. The cross-head displacement speed was set as 0.2 mm/min in the three-point bending tests following ASTM D790. The deformation from the testing fixtures was measured using a rigid steel block with dimensions of roughly 60 mm × 40 mm × 10 mm under load up to 813 N and then subtracted from the measured results using Equation (1). The microhardness was measured by Vicker's indentation using a Buehler micro-hardness tester at a load of 500 g force and a dwell time of 15 s.

The deformation and load data were collected to calculate flexural stress σ, Young's modulus E, and strain ε with the following equations:

$$\sigma = 3PL/(2bh^2) \tag{1}$$

$$E = \sigma/\varepsilon \tag{2}$$

$$\varepsilon = 6h\delta/L^2 \tag{3}$$

where P is the load upon failure, L is the span length, b is the sample width, h is the sample thickness, and δ is the displacement at the sample center. Five samples of each microstructure type were tested to determine the variability in the mechanical properties.

The dependence of Young's modulus and bending strength on sample porosity can be approximated using the following equations [49]:

$$E = E_o(1 - 1.9P + 0.9P^2) \tag{4}$$

$$\sigma_{fs} = \sigma_o \exp(-nP) \tag{5}$$

where E_o and σ_o are the material Young's modulus and bending strength without porosity, respectively, the predicted modulus and strength are E and σ_{fs}, P is porosity, and n is a factor that needs to be determined.

To find the best fit of n in Equation (5), we take the natural logarithm of Equation (5) and perform linear regression for different n values to find the n that best fits the measured values.

$$\ln(\sigma_{fs}) = \ln(\sigma_o) - nP \tag{6}$$

The relationship between hardness and porosity can be approximated by the following equation [50]:

$$H = H_o(1 - P)^{n'} \tag{7}$$

where H denotes material hardness at porosity P, and H_o is the hardness without porosity. The value of n' is an empirical constant that depends on the material and the porosity type. The n' value can be obtained by taking the natural logarithm on both sides of Equation (7) and performing a linear regression:

$$\ln(H) = \ln(H_o) + n'\ln(1 - P) \tag{8}$$

3. Results and Discussion

3.1. Microstructure and Porosity

In the previous study [48], we analyzed the influence of varying pore former sizes and volume fractions on material properties directly affecting solid oxide cell electrochemical performance. These properties encompassed the shrinkage rate of the sintered support relative to the green body size, surface roughness, porosity, surface area to volume ratio, mass gain after oxidation, and gas permeability. Pore former particle sizes considered were 20, 40, 60, and 90 µm, with volume fractions ranging from 25 vol% to 55 vol% in 10 vol% increments. It was observed that pore formers larger than 20 µm exhibited relatively consistent shrinkage, irrespective of volume fraction. In comparison, for the 20 µm pore former, the volume fraction had a proportional impact on shrinkage. Our previous findings concluded that the 60 µm pore former at 45 vol% yielded the most balanced results in the properties studied. Therefore, for this study, we selected 20 and 60 µm pore formers (PF20 and PF60, respectively), chosen for their distinct sintering characteristics, to study the effect of volume fraction on mechanical properties. Samples sintered without pore former were also included as a baseline comparison. Table 2 summarizes the microstructural characteristics of these three types of specimens. It should be noted that samples made without pore formers have primarily closed porosity, which does not contribute to oxidation. Hence, the perimeter/area ratio was not measured for those samples.

Table 2. Structural features of sintered supports made with various pore former contents.

	No Pore Former	**PF20**				**PF60**		
		25%	**35%**	**45%**	**55%**	**35%**	**45%**	**55%**
Shrinkage (%)	17.2	17.5	20.5	22.7	25.0	16.1	16.5	15.9
Porosity (%)	0.00775	8.56	14.2	18.5	28.9	28.4	35.5	46.5
Perimeter/area ratio (μm^{-1})	n/a	0.03	0.05	0.06	0.09	0.04	0.06	0.07

Figure 1 shows cross-sectional images of samples sintered without pore former (a) and with 55 vol% PF20 (b) and 55 vol% PF60 (c), respectively. In the images, the samples were oriented the same way as they were placed in the furnace during sintering. The top surface in each image is the side of the specimen facing the gas flow, and the bottom of each specimen in the image is the side facing the alumina plate. Even in the specimen made without pore former, the material still has some minor closed pores with a porosity gradient from the top to the bottom of the image. The top side, closer to the gas flow, has less porosity, and the deeper parts have more porosity. Substrates made with pore former have a connected porosity network, as shown in Figure 1b,c. For PF20 substrates, the pores in many locations are narrow and elongated/connected over a distance corresponding to 5 or more pore former particle diameters. For PF60 substrates, the pores have more spherical shapes, with throats connecting a smaller number of particles. The backscattered electron image shows a uniform gray scale over the metal part, indicating uniform atomic mass distribution over the metallic phase.

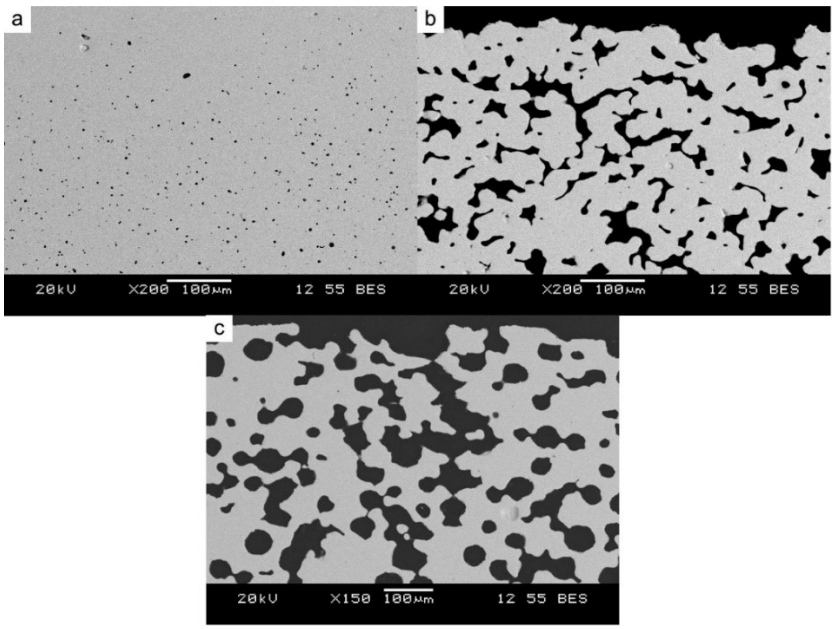

Figure 1. Backscattered SEM images of 430L stainless steel supports sintered at 1200 °C for 4 h, made with (**a**) no pore former, showing small pores; (**b**) 55 vol% PF20, showing irregular pores; (**c**) 55 vol% PF60, showing larger spherical pores.

Figure 2 shows the porosity of PF60 (a and b) and PF20 (c and d) supports after three-point bending (TPB) deformation in the tensile and compressive loaded regions. Based on image analysis at both tensile and compressive deformation sites, the porosity of the PF20 and PF60 samples changed by approximately 3% at both tensile and compressive regions, with porosity decreasing in the compressive regions and increasing in the tensile regions.

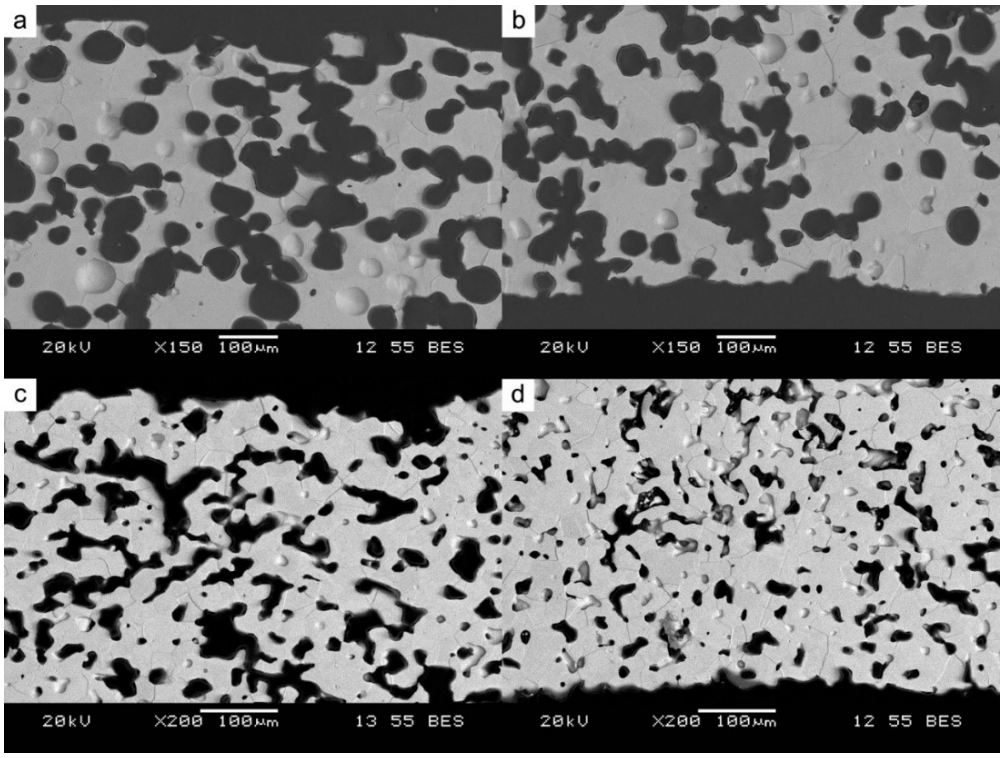

Figure 2. SEM images of porous samples after TPB tests, showing (**a**) tensile and (**b**) compressive deformation of a PF60 support and (**c**) tensile and (**d**) compressive deformation of a PF20 support. The tensile deformation in (**a**,**c**) shows horizontal elongation and enlargement of porosity, while the compression reduces the observable porosity in (**b**,**d**).

The porosity gradient in the sample without pore former is unexpected and is not likely related to a temperature gradient within the sample in the vertical direction. The sample thickness is approximately 1.5 mm, and the distance is too small for a temperature gradient that can cause a significantly different extent of sintering, considering the high thermal conductivity of stainless steel. The heating elements around the process tube are arranged vertically and parallel to each other, so the porosity gradient should be horizontal if there is any temperature gradient from the heating element. When comparing the dense sample bottom side and top side, the thickness of the pore-free layer is greater at the top side than at the bottom side in Figure 3a. From the cross-sectional view of the etched sample in Figure 3b, the upper part close to the gas side has larger grains than the part deeper into the material. This grain size distribution confirms that the upper part has a higher sintering extent. A similar region with only small pores can also be observed in a sample sintered with 55 vol% PF60 pore formers in small regions that lacked porosity from pore former, as shown in Figure 3c. From sintering theory [51] and as shown in an example of previously reported literature results [52], grain size growth is the final stage of sintering, and the enlargement of grains can be slowed down by impurities present at grain boundaries. We suspect that the residual porosity is due to the incomplete reduction of Cr oxide created from the organic removal step. According to thermogravimetric analysis of the green tape in earlier work [33], at 400 °C, the steel particles were already showing some mass gain at the temperature at which the tube furnace atmosphere was switched from air to hydrogen. A colour change due to oxidation could also be seen by visual observation. At higher temperatures, from above 700 °C, hydrogen can reduce chromium oxide back to chromium, but that requires very dry hydrogen; even at the sintering temperature, the partial pressure of water needs to be less than 20 Pa for the reduction to happen [51]. The steel exposed to higher purity hydrogen flow can experience a reduction of its surface chromium oxide scale. In contrast, inner particles cannot be reduced because of diffusion limitations of both hydrogen going in and water vapour coming out. The introduced porosity enables a more complete reduction of chromium oxide throughout the supports, hence a more uniform grain size and denser structure. Consequently, unreduced chromium oxide could be responsible for smaller grain size and higher residual porosity due to its higher sintering temperature compared to the surrounding ferrite phase.

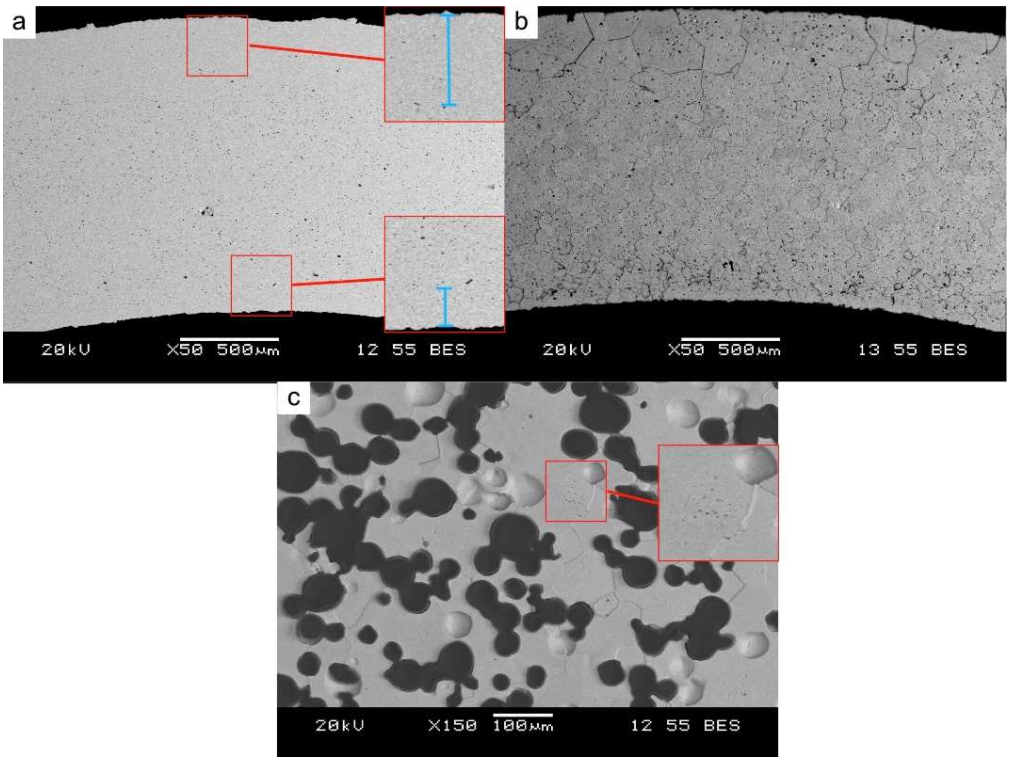

Figure 3. SEM images of sample cross-sections showing that residual porosity from inter-particle spaces is not uniformly distributed. (**a**) A thicker, dense layer (thickness indicated in blue lines) on the side of specimens adjacent to the gas flow during sintering (top) compared to the alumina plate side (bottom); (**b**) larger grain sizes at the top side compared to the center after etching; (**c**) residual porosity at locations in a 55 vol% PF60 sample where no pore former was present.

3.2. Mechanical Properties

All the tested samples showed ductile properties with a long plastic deformation region upon load. Figure 4 shows a typical stress-strain curve from a 35 vol% PF20 sample. Considering the brittle nature of deposited ceramic layers on metal supports as well as the flexural strain value limitation in Equation (3), the substrate elastic modulus is more relevant to the failure of the ceramic layers than the flexural strength. If the specimen fails below 5% strain, the maximum stress is taken as the flexural strength; otherwise, the stress at a strain limit of 5% is taken as the flexural strength, as specified in ASTM D790. Any ceramic layer would have already failed before the metal support finally reaches the maximum strain.

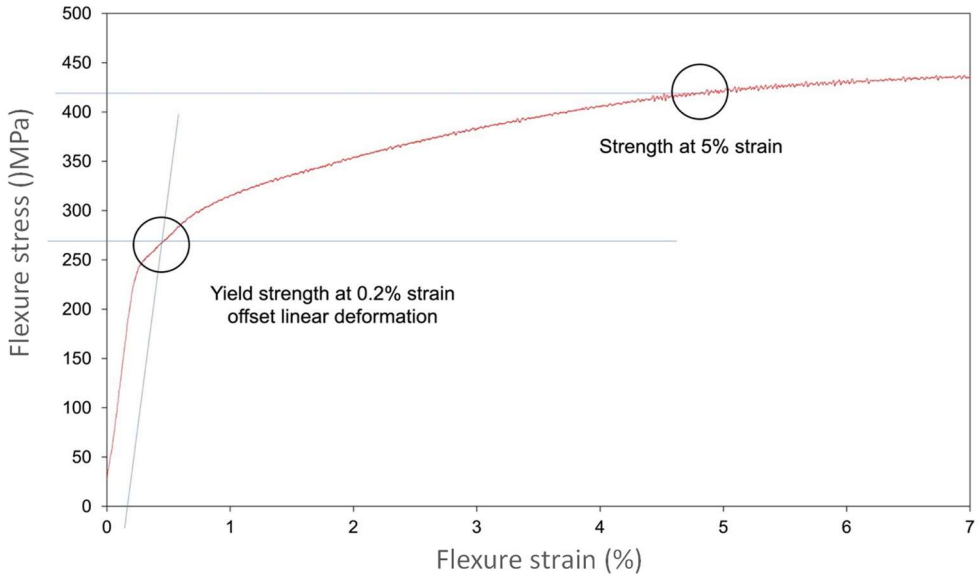

Figure 4. A typical curve of flexure stress *vs.* flexure strain for a 35 vol% PF20 sample with a long strain until the testing fixture has reached its maximum displacement range. The yield strength and the strength at the 5% strain limit are evaluated as per ASTM D790.

The Young's modulus (E) and yield strength of 430L SS have been reported in the literature as 200 GPa and 345 MPa, respectively [53]. Regarding the sample prepared without pore former in the present study, the tested samples have a lower Young's modulus and higher yield strength of 163 GPa and 385 MPa, respectively. Therefore, the TPB tests of the relatively small and thin samples (~1.5 mm) could only be used to estimate the changing trend of the mechanical properties affected by the processing parameters mentioned above (*i.e.*, for relative comparisons).

For Young's modulus, there is an overall decreasing trend for PF20 samples with increasing porosity, despite the midpoint having larger variations, as shown in Figure 5a. There is no clear trend for Young's modulus of PF60 samples, which appears to fluctuate between low values of 40 and 60 GPa with large standard deviations of approximately 20 GPa. The yield strength results are shown in Figure 5b. A clear decreasing trend starts from 385 MPa for the no-pore-former sample down to 118 MPa for the sample with the highest porosity, and most data points have relatively small standard deviations. Despite the different pore former sizes, 55 vol% PF20 and 35 vol% PF60 substrates had similar final porosity, and the yield strengths were also similar, as seen in Figure 5b. While Young's modulus values have large standard deviations, the yield strength values exhibit more consistent changes as a function of porosity.

Figure 5c shows the results of the flexural strength evaluated at the 5% strain limit as specified in ASTM D790. Like the flexural yield strength (Figure 5b), the data points also show a decreasing trend from 633 MPa with no pore former to 164 MPa at 46.5% porosity. The PF60 samples with approximately 35% porosity had a larger standard deviation than the others, although the reasons for this difference are unclear.

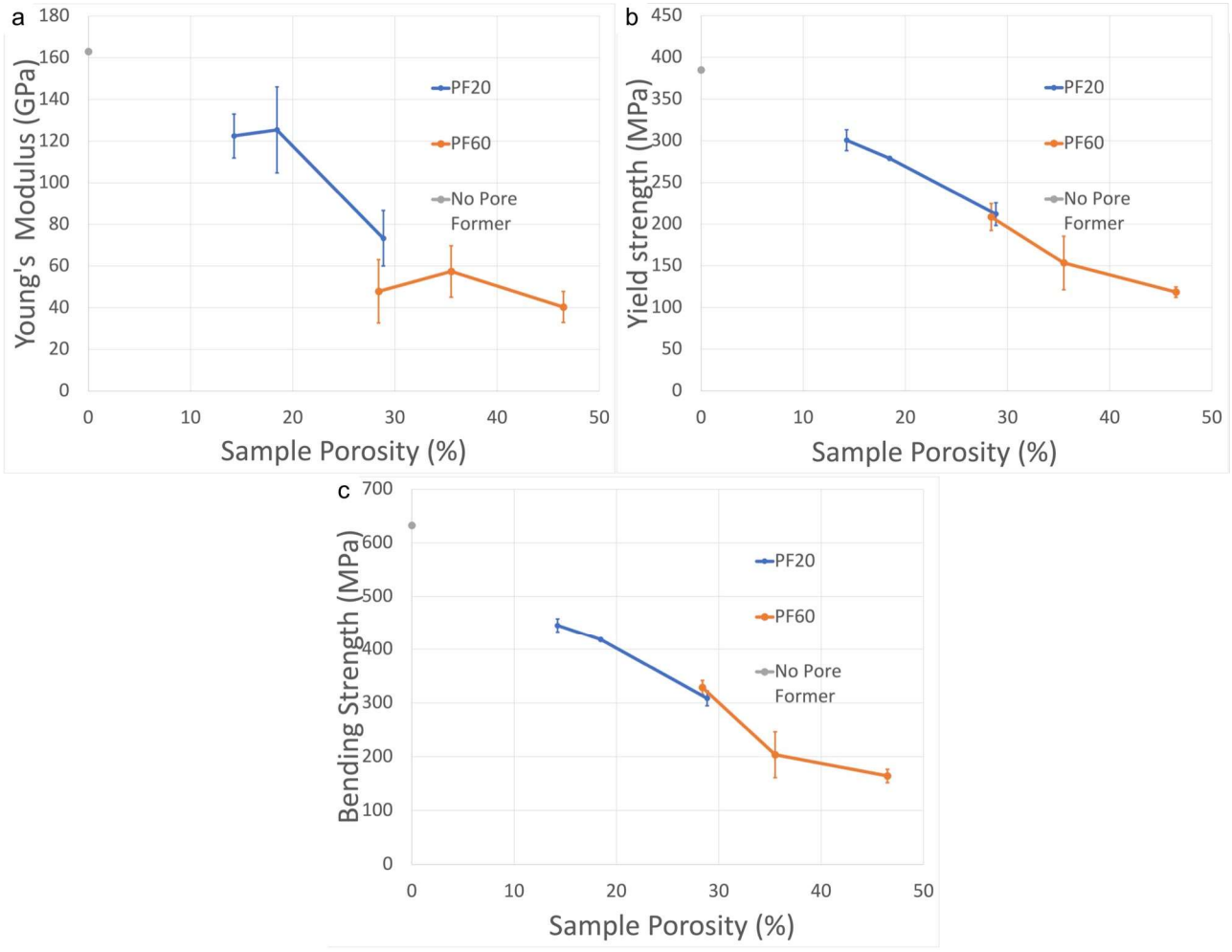

Figure 5. (**a**) Young's modulus, (**b**) yield strength, and (**c**) bending strength at 5% strain limit or maximum strength if failed before the limit as a function of sample porosity and pore former size.

One interesting observation is that the modulus of PF60 with 35 vol% pore former is smaller than the modulus with 45 vol%, and smaller than that of the PF20 with 55% pore former. In yield strength and bending strength measurements, the value of PF60 at 35 vol% is similar to that of PF20 at 55%. It is possible that the more isolated pores resulting from low levels of the PF60 pore former resulted in disproportionate levels of deformation in isolated areas of the specimens, compared to the more uniformly distributed porosity resulting from the PF20 pore formers. However,

the use of machine displacement for the evaluation of sample strain may have also introduced some scatter in the measured values, despite the machine calibration procedure with a large, high-stiffness specimen.

For PF20 samples, Young's modulus was closely approximated by Equation (4), the mean squared error (MSE) is 91.89, and R^2 is 0.909. For PF60, the MSE is 458.4 and R^2 is 0.816, with the first data point having the most significant disagreement. The results imply that using Equation (4) to approximate Young's modulus relation with porosity is good for fine and uniformly distributed samples.

For PF20 samples, the n that gives the best fit is 2.43, and R^2 is 0.994. For PF60 samples, the n that gives the best fit is 2.88, and R^2 is 0.964. The larger n for larger PF60 suggests that the larger pore former has a more significant impact on the sample bending strength, and this trend agrees with the trend from other reported material [45].

3.3. Micro-Hardness

The microhardness of the test samples is shown in Figure 6. As expected, the sample fabricated without pore former has the highest hardness value of 133 HV due to the presence of the lowest porosity (Figure 1a). As the porosity increases, the hardness decreases, being similar to the change in strength (Figure 5b,c). The PF20 samples start at approximately 14% porosity with a hardness just below 80 HV; the hardness decreases as the sample porosity increases. Notably, the PF60 samples have larger error bars, especially in the lowest porosity condition.

Figure 6 shows the micro hardness of both PF20 and PF60 with respect to various porosities. Although PF20 and PF60 seem connected, PF20 has a more gradual decrease than PF60. The finer pore former in PF20 leads to a more uniform distribution of smaller pores throughout the material. During the hardness test, the indenter was more likely to contact a representative combination of material and voids, as shown in Figure 6b. This led to a measurement that reflects both the solid matrix and the porosity with a relatively smaller standard deviation in the data points.

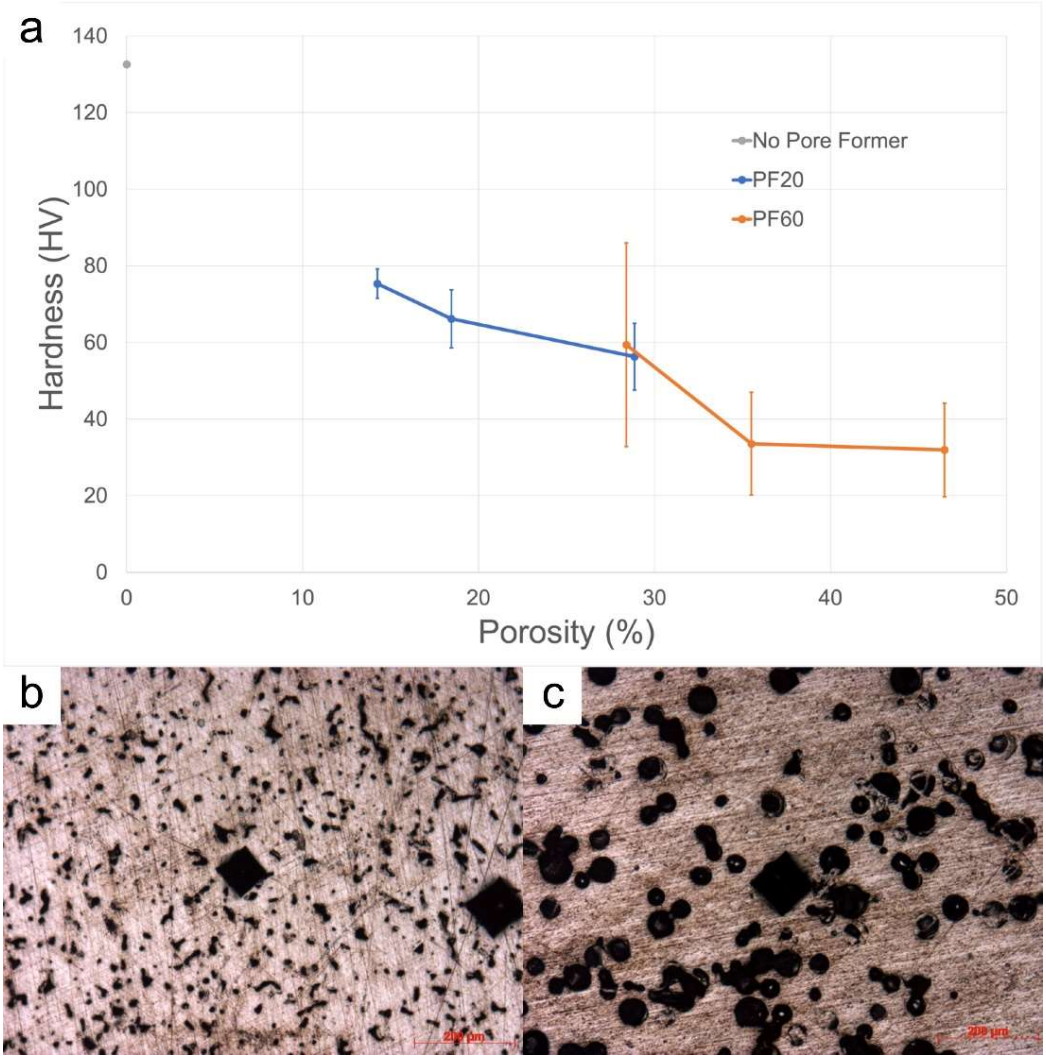

Figure 6. (**a**) Micro-hardness determined at a load of 500 g as a function of porosity, along with typical images of the indentation of samples made with 35 vol% PF20 (**b**) and PF60 (**c**).

For PF60 samples made with a larger pore former, the porosity is less evenly distributed, resulting in larger but fewer voids. This increases the likelihood that an indentation test will strike an area of dense material or large voids, as shown in two different-sized dents in Figure 6c. This can cause greater variation in hardness measurements, as reflected by the wider error bars at higher porosities for PF60. With the larger PF60, a higher volume fraction is required to increase the chance for the indenter to contact a representative region with both bulk material and porosity present.

For PF20, the best-fit *n*' is 2.87, with R^2 being 0.899; for PF60, the best-fit *n*' is 2.53, with R^2 being 0.926. Because PF20 samples have larger *n*', their hardness reaches flatter portions of the curve faster than PF60 at smaller porosity; on the other hand, the PF60 curve becomes steeper than the PF20 curve at higher porosity. Different *n*' values suggest that different pore sizes had a different impact on the material hardness.

3.4. Electron Backscatter Diffraction

Three EBSD crystal orientation maps are shown in Figure 7. for pore former samples, with crystal orientation relative to the sample reference plane visualized by inverse pole figures (IPF). The images show isotropic characteristics for the porous and non-porous samples, as the mapped grains have no dominant orientation amongst the <001>, <101>, and <111> poles. Despite the tape casting process, which applied a linear motion to the suspended particles, the sintered material does not show anisotropy. The grain orientation is not impacted by tape casting. Since isotropic materials have no preferred grain orientation, the TPB test results would likely have less variability than samples with a preferred orientation, and the accuracy and reproducibility of the mechanical data are, therefore, expected to be reasonably good.

Figure 8 shows the kernel average misorientation (KAM) maps from the EBSD analysis of samples after the TPB test. The nonporous samples exhibit a uniform strain distribution in both compression and tension zones, with a stress-free layer at the center (Figure 8a). Above this central layer, the material experiences compressive stress, while the region below is subjected to tensile stress due to the shear forces generated by bending. This balanced distribution suggests a symmetrical deformation pattern typical of bending stress profiles in nonporous structures.

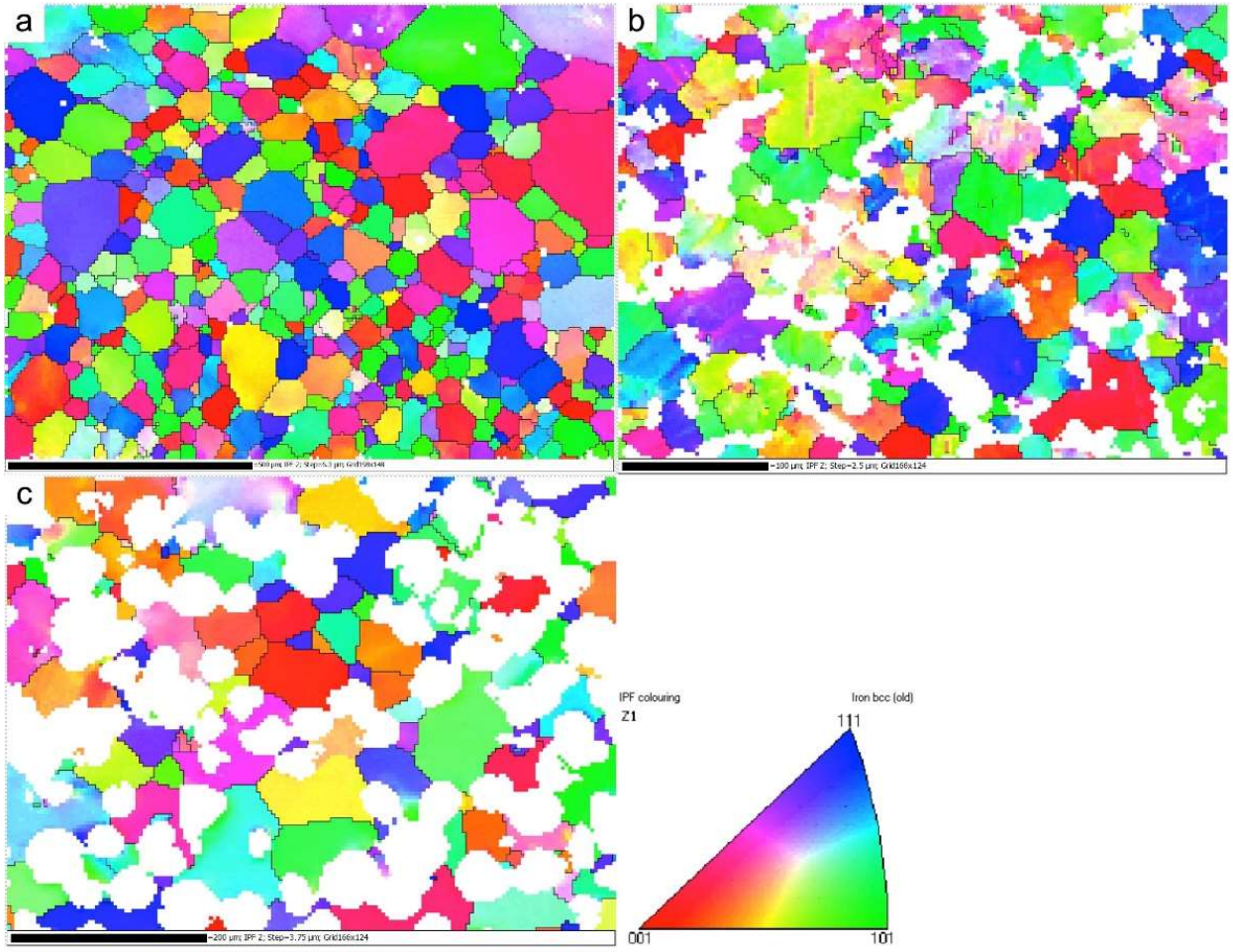

Figure 7. EBSD IPF maps of three-point bending tested samples prepared with (**a**) no pore former, (**b**) with 55 vol% PF20, and (**c**) with 55 vol% PF60 after TPB testing.

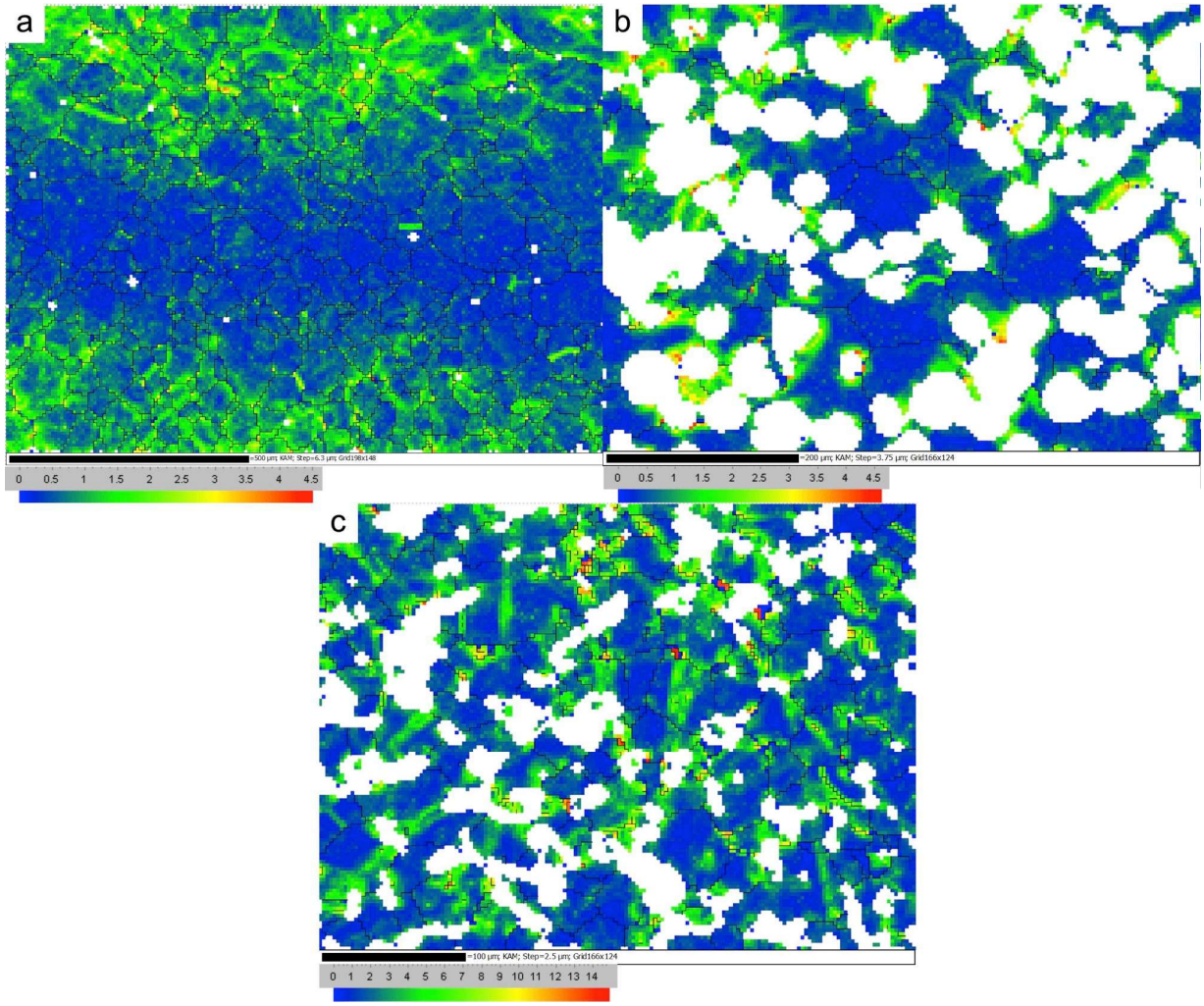

Figure 8. Kernel average misorientation (KAM) maps of post-TPB test samples prepared with (**a**) no pore former, (**b**) 55 vol% PF60, and (**c**) 55 vol% PF20.

In contrast, the porous samples demonstrate strain localization primarily around the solid throat regions caused by porosity, which extends through the entire sample thickness. One difference between the PF20 and PF60 was that in PF20, more deformation went through grains instead of localizing at the throats, leading to fewer regions with local stress concentration. Denser areas within the porous samples exhibit reduced deformation, suggesting that the porosity contributes to an uneven strain distribution, with a lower strain in denser regions and increased concentration in areas where porosity-induced throats occur.

These results provide preliminary insight into the influence of porosity on the mechanical properties of stainless steel at room temperature. Porous stainless steel with the properties reported here has been shown to be viable as a support for SOCs operating at 750 °C under conditions with minimal external mechanical loading. However, due to the drop in yield strength as steel is operated at higher temperatures, additional care must be utilized in designing a porous ferritic steel structure to be used at elevated temperatures in applications involving mechanical loads, such as in transportation applications. For example, heat treatment such as martensitic quenching and tempering may be helpful in starting the 430L stainless steel to be used at a higher room temperature yield strength, so that after the reduction resulting from the combination of the porous structure and the high operating temperature, any mechanical loads applied during operation can still be withstood by the heat-treated material. Alternatively, components exterior to the cell, such as the interconnects or suspension system surrounding the stack in a transportation application, must be designed to minimize the mechanical load on the stack, even when relatively strong stainless steel is used. More testing of full-scale cells and stacks with interconnects at higher operating temperatures will be required to assess in greater detail the levels of mechanical stresses that will be imposed on the stack and to determine the additional strengthening heat treatments that may be required prior to the fabrication of the SOC components on the porous metal support structures.

4. Conclusions

This work shows that sintered porous 430L stainless steel produced by powder metallurgy has sufficient mechanical strength as a metal support for the SOC application. The material shows very ductile behaviour. The yield strength, often lower than the flexural strength, was compared to the requirement for PEMFC bipolar plates and found to be greater than the 59 MPa requirement for the vehicle application. All the tested specimens, ranging widely in porosity from nearly 0 to 46.5%, met this requirement. There is a significant drop in yield strength with increasing porosity from 385 to 118 MPa over this wide porosity range. The EBSD analysis shows that the linear shear motion applied to the slurry does not create any preferred orientation of the material. Kernel average misorientation mapping suggests that the throats created by the porosity have the most misorientation during three-point bending loading, which implies that those regions experience the highest degree of deformation. This study is limited to room temperature, which is far from typical SOC operation temperature. Hence, future testing at higher temperatures is necessary. However, given the relationship between porosity and mechanical properties tested in this study, the high-temperature mechanical properties may be predictable from dense 430L samples measured at higher temperatures.

Acknowledgments

This study was funded by the Natural Sciences and Engineering Research Council of Canada (NSERC) and Volta Energy.

Author Contributions

Y.Y.: conceptualization, data curation, validation, formal analysis, methodology, visualization, writing—original draft. D.B.: data curation, validation, methodology, visualization, writing— review and editing. O.K.: conceptualization, funding acquisition, methodology, resources, supervision, project administration, writing—review and editing. D.C.: funding acquisition, methodology, resources, supervision, project administration, writing—review and editing. All authors have read and agreed to the published version of the manuscript.

Ethics Statement

Not applicable.

Informed Consent Statement

Not applicable.

Funding

This study was funded by the Natural Sciences and Engineering Research Council of Canada (NSERC) grant number ALLRP 584794-23 and Volta Energy.

Declaration of Competing Interest

The authors declare that they have no known competing financial interests or personal relationships that could have appeared to influence the work reported in this paper.

Data Availability

Data will be made available on request.

References

1. Paulina J, Suzana Kahn R, Peter N, Subash D, Ogheneruona E. D, Tsutomu K. et al. *Climate Change 2022—Mitigation of Climate Change*, 1st ed.; Intergovernmental Panel on Climate Change (IPCC), Ed.; Cambridge University Press: Cambridge, UK, 2023; Ch. 10. doi:10.1017/9781009157926.012.
2. Tokimatsu K, Konishi S, Ishihara K, Tezuka T, Yasuoka R, Nishio M. Role of innovative technologies under the global zero emissions scenarios. *Appl. Energy* **2016**, *162*, 1483–1493. doi:10.1016/j.apenergy.2015.02.051.
3. Møller KT, Jensen TR, Akiba E, Li H. Hydrogen—A sustainable energy carrier. *Prog. Nat.Sci. Mater. Int.* **2017**, *27*, 34–40. doi:10.1016/j.pnsc.2016.12.014.

4. Yi H-S, Jeong J-B, Cha S-W, Zheng C-H. Optimal component sizing of fuel cell-battery excavator based on workload. *Int. J. Precis. Eng. Manuf. -Green Technol.* **2018**, *5*, 103–110. doi:10.1007/s40684-018-0011-z.
5. Offer GJ, Howey D, Contestabile M, Clague R, Brandon NP. Comparative analysis of battery electric, hydrogen fuel cell and hybrid vehicles in a future sustainable road transport system. *Energy Policy* **2010**, *38*, 24–29. doi:10.1016/j.enpol.2009.08.040.
6. Tsakiris A. Analysis of hydrogen fuel cell and battery efficiency. In Proceedings of the World Sustainable Energy Days 2019. Young Energy Researchers Conference, Wels, Austria, 27 February–1 March 2019.
7. Turner CH, Wang X, Lau KC, An W, Dunlap BI. Atomistic Modeling of Solid Oxide Fuel Cells. *Annu. Rep. Comput. Chem.* **2010**, *6*, 201–234. doi:10.1016/S1574-1400(10)06011-1.
8. Luo Y, Jiao K. Cold start of proton exchange membrane fuel cell. *Prog. Energy Combust. Sci.* **2018**, *64*, 29–61. doi:10.1016/j.pecs.2017.10.003.
9. van Veldhuizen BN, van Biert L, Amladi A, Woudstra T, Visser K, Aravind PV. The effects of fuel type and cathode off-gas recirculation on combined heat and power generation of marine SOFC systems. *Energy Convers. Manag.* **2023**, *276*, 116498. doi:10.1016/J.ENCONMAN.2022.116498.
10. Jeerh G, Zhang M, Tao S. Recent progress in ammonia fuel cells and their potential applications. *J. Mater. Chem. A Mater.* **2021**, *9*, 727–752. doi:10.1039/D0TA08810B.
11. Zhao Y, Setzler BP, Wang J, Nash J, Wang T, Xu B, et al. An Efficient Direct Ammonia Fuel Cell for Affordable Carbon-Neutral Transportation. *Joule* **2019**, *3*, 2472–2484. doi:10.1016/j.joule.2019.07.005.
12. Zhang X, Zhang Z, Zhou Z. MXene-based materials for electrochemical energy storage. *J. Energy Chem.* **2018**, *27*, 73–85. doi:10.1016/j.jechem.2017.08.004.
13. Chen Y, Zhang Y, Lin Y, Yang Z, Su D, Han M, et al. Direct-methane solid oxide fuel cells with hierarchically porous Ni-based anode deposited with nanocatalyst layer. *Nano Energy* **2014**, *10*, 1–9. doi:10.1016/j.nanoen.2014.08.016.
14. Liu F, Gao Y, Li J, Wei T, Ye Z, Zhang T, et al. Direct ethanol solid oxide fuel cells integrated with internal reforming for renewable power generation. *Sep. Purif. Technol.* **2022**, *298*, 121678. doi:10.1016/j.seppur.2022.121678.
15. Zhan Z, Barnett SA. An Octane-Fueled Solid Oxide Fuel Cell. *Science* **2005**, *308*, 844–847. doi:10.1126/science.1109213.
16. Chi Y, Li P, Lin J, Li J, Mu S, Song Y. Fast and safe heating-up control of a planar solid oxide cell stack: A three-dimensional model-in-the-loop study. *J. Power Sources* **2023**, *560*, 232655. doi:10.1016/j.jpowsour.2023.232655.
17. Faes A, Hessler-Wyser A, Zryd A, Van herle J. A Review of RedOx Cycling of Solid Oxide Fuel Cells Anode. *Membranes* **2012**, *2*, 585–664. doi:10.3390/membranes2030585.
18. Brandon NP, Blake A, Corcoran D, Cumming D, Duckett A, El-Koury K, et al. Development of Metal Supported Solid Oxide Fuel Cells for Operation at 500–600 °C. *J. Fuel Cell Sci. Technol.* **2004**, *1*, 61–65. doi:10.1115/1.1794709.
19. Bance P, Brandon NP, Girvan B, Holbeche P, O'Dea S, Steele BCH. Spinning-out a fuel cell company from a UK University—2 years of progress at Ceres Power. *J. Power Sources* **2004**, *131*, 86–90. doi:10.1016/j.jpowsour.2003.11.077.
20. Metcalfe TC. Development and Characterization of Nickel and Yttria-Stabilized Zirconia Anodes for Metal-Supported Solid Oxide Fuel Cells Fabricated by Atmospheric Plasma Spraying. Doctorate, University of Toronto, Toronto, ON, Canada, 2013. Available online: https://hdl.handle.net/1807/43667 (accessed on 19 July 2024).
21. Rose L, Kesler O, Decès-Petit C, Troczynski T, Maric R. Characterization of porous stainless steel 430 for low- and intermediate-temperature solid oxide fuel cell (SOFC) substrates. *Int. J. Green Energy* **2009**, *6*, 638–645. doi:10.1080/15435070903372510.
22. Dogdibegovic E, Wang R, Lau GY, Karimaghaloo A, Lee MH, Tucker MC. Progress in durability of metal-supported solid oxide fuel cells with infiltrated electrodes. *J. Power Sources* **2019**, *437*, 226935. doi:10.1016/j.jpowsour.2019.226935.
23. Marr M, Kesler O. Permeability and microstructure of suspension plasma-sprayed YSZ electrolytes for SOFCs on various substrates. *J. Therm. Spray Technol.* **2012**, *21*, 1334–1346. doi:10.1007/s11666-012-9829-z.
24. Brandner M, Bram M, Froitzheim J, Buchkremer HP, Stöver D. Electrically Conductive Diffusion barrier layers for Metal-Supported SOFC. *Solid State Ion* **2008**, *179*, 1501–1504. doi:10.1016/j.ssi.2008.03.002.
25. Tucker MC. Dynamic-temperature operation of metal-supported solid oxide fuel cells. *J. Power Sources* **2018**, *395*, 314–317. doi:10.1016/j.jpowsour.2018.05.094.
26. Rufner J, Gannon P, White P, Deibert M, Teintze S, Smith R, et al. Oxidation behavior of stainless steel 430 and 441 at 800 °C in single (air/air) and dual atmosphere (air/hydrogen) exposures. *Int. J. Hydrogen Energy* **2008**, *33*, 1392–1398. doi:10.1016/j.ijhydene.2007.12.067.
27. Reisert M, Berova V, Aphale A, Singh P, Tucker MC. Oxidation of porous stainless steel supports for metal-supported solid oxide fuel cells. *Int. J. Hydrogen Energy* **2020**, *45*, 30882–30897. doi:10.1016/j.ijhydene.2020.08.015.
28. Gschiel H, Gierl-Mayer C, Danninger H, Larsson P-O, Vidarsson H. Manufacturing and microstructure of porous metal supports for a solid oxide fuel cell. *Powder Metall.* **2015**, *58*, 178–181. doi:10.1179/0032589915Z.000000000237.
29. Wang H, Xie S, Lai W, Liu X, Chen C, Meng G. Preparation and characterization of perovskite ceramic powders by gelcasting. *J. Mater. Sci.* **1999**, *34*, 1163–1167. doi:10.1023/A:1004592418985/METRICS.
30. Qiang F, Sun K, Zhang N, Le S, Zhu X, Piao J. Optimization on fabrication and performance of A-site-deficient $La_{0.58}Sr_{0.4}Co_{0.2}Fe_{0.8}O_{3-\delta}$ cathode for SOFC. *J. Solid State Electrochem.* **2009**, *13*, 455–467. doi:10.1007/s10008-008-0581-8.

31. Nie L, Sun Q, Liu Z, Liu M. Graded porous solid oxide fuel cells fabricated by multilayer tape casting and co-firing progress. *Int. J. Hydrogen Energy* **2015**, *40*, 16503–16508. doi:10.1016/J.IJHYDENE.2015.10.007.
32. Nguyen XV, Chang CT, Jung GB, Chan SH, Huang WCW, Hsiao KJ, et al. Effect of sintering temperature and applied load on anode-supported electrodes for SOFC application. *Energies* **2016**, *9*, 701. doi:10.3390/en9090701.
33. Yan Y, Kesler O. Discover Materials Fabrication of flat stainless steel substrates with improved oxidation behavior for metal-supported solid oxide cells using aqueous tape casting. *Discov. Mater.* **2023**, *3*, 28. doi:10.1007/s43939-023-00063-5.
34. Wei Z, Oliveira M, Laizhu J, Guangwei F, Junyan F. Nb Microalloyed Modern Ferritic Stainless Steel. In *HSLA Steels 2015, Microalloying 2015 & Offshore Engineering Steels 2015*; The Chinese Society of Metals, Chinese Academy of Engineering, Eds.; Springer: Hangzhou, China, 2015; pp. 887–894.
35. Harris J, Yan Y, Bateni R, Kesler O. Degradation of $La_{0.6}Sr_{0.4}Co_{0.2}Fe_{0.8}O_{3-\delta}$–$Ce_{0.8}Sm_{0.2}O_{1.9}$ Cathodes on Coated and Uncoated Porous Metal Supports. *Fuel Cells* **2016**, *16*, 319–329. doi:10.1002/fuce.201500139.
36. Yan Y, Bateni R, Harris J, Kesler O. Fabrication of reactive element oxide coatings on porous ferritic stainless steel for use in metal-supported solid oxide fuel cells. *Surf. Coat. Technol.* **2015**, *272*, 415–427. doi:10.1016/j.surfcoat.2015.03.041.
37. Shong W-J, Liu C-K, Yang P. Effects of electroless nickel plating on 441 stainless steel as SOFC interconnect. *Mater. Chem. Phys*. **2012**, *134*, 670–676. doi:10.1016/j.matchemphys.2012.03.049.
38. Arevalo-Quintero O, Kesler O. Development of Bi-layer Metal Substrate Architectures for Suspension Plasma Sprayed Solid Oxide Fuel Cells. *Fuel Cells* **2018**, *18*, 466–475. doi:10.1002/fuce.201700187.
39. Tucker MC. Progress in metal-supported solid oxide fuel cells: A review. *J. Power Sources* **2010**, *195*, 4570–4582. doi:10.1016/j.jpowsour.2010.02.035.
40. Marr M, Kuhn J, Metcalfe C, Harris J, Kesler O. Electrochemical performance of solid oxide fuel cells having electrolytes made by suspension and solution precursor plasma spraying. *J. Power Sources* **2014**, *245*, 398–405. doi:10.1016/j.jpowsour.2013.06.092.
41. Hui R, Wang Z, Kesler O, Rose L, Jankovic J, Yick S, et al. Thermal plasma spraying for SOFCs: Applications, potential advantages, and challenges. *J. Power Sources* **2007**, *170*, 308–323. doi:10.1016/j.jpowsour.2007.03.075.
42. Meier GH, Jung K, Mu N, Yanar NM, Pettit FS, Pirón Abellán J, et al. Effect of alloy composition and exposure conditions on the selective oxidation behavior of ferritic Fe-Cr and Fe-Cr-X alloys. *Oxid. Met.* **2010**, *74*, 319–340. doi:10.1007/s11085-010-9215-5.
43. Molin S, Kusz B, Gazda M, Jasinski P. Evaluation of porous 430L stainless steel for SOFC operation at intermediate temperatures. *J Power Sources* **2008**, *181*, 31–37. doi:10.1016/j.jpowsour.2007.10.009.
44. Tammas-Williams S, Withers PJ, Todd I, Prangnell PB. The Influence of Porosity on Fatigue Crack Initiation in Additively Manufactured Titanium Components. *Sci. Rep*. **2017**, *7*, 7308. doi:10.1038/s41598-017-06504-5.
45. Das D, Lucio MDS, Kultayeva S, Kim Y-W. Effect of pore size on the flexural strength of porous silicon carbide ceramics. *Open Ceram.* **2024**, *17*, 100521. doi:10.1016/j.oceram.2023.100521.
46. Planes E, Flandin L, Alberola N. Polymer Composites Bipolar Plates for PEMFCs. *Energy Procedia* **2012**, *20*, 311–323. doi:10.1016/j.egypro.2012.03.031.
47. Chang C-L, Tsai C-H, Fu C-Y, Yang C-S, Yang S-F, Lee R-Y. Fabrication and Characterization of Metal-Supported Solid Oxide Fuel Cell Fabricated by Atmospheric Plasma Spraying. *ECS Trans*. **2019**, *91*, 855–865. doi:10.1149/09101.0855ecst.
48. Yan Y, Kesler O. Evaluation of Pore Former Size and Volume Fraction on Tape Cast Porous 430 Stainless Steel Substrates for Plasma Spraying. *Materials* **2024**, *17*, 5408.
49. Callister WD, Rethwisch DG. *Materials Science and Engineering an Introduction*, 10th ed.; Wiley: Danvers, MA, USA, 2018.
50. Luo J, Stevens R. Porosity-dependence of elastic moduli and hardness of 3Y-TZP ceramics. *Ceram. Int.* **1999**, *25*, 281–286.
51. ASM International Handbook Committee. *ASM Handbook, Volume 7: Powder Metallurgy, Vol. 07*; ASM International: Materials Park, OH, USA, 2015.
52. Murugaiah A, Souchet A, El-Raghy T, Radovic M, Sundberg M, Barsoum MW. Tape Casting, Pressureless Sintering, and Grain Growth in Ti_3SiC_2 Compacts. *J. Am. Ceram. Soc.* **2004**, *87*, 550–556. doi:10.1111/j.1551-2916.2004.00550.x.
53. Harvey PD. (Ed.). *Engineering Properties of Steel*; American Society for Metals: Materials Park, OH, USA, 1982.